Nontrivial superconductivity in topological MoTe$_{2-x}$S$_x$ crystals

Yanan Li[a,b,c,1], Qiangqiang Gu[a,b,1], Chen Chen[d,e,1], Jun Zhang[d,e], Qin Liu[d,e,f], Xiyao Hu[a], Jun Liu[g], Yi Liu[a,b], Langsheng Ling[g], Mingliang Tian[g], Yong Wang[h], Nitin Samarth[c], Shiyan Li[d,e,i], Tong Zhang[d,e,i,2], Ji Feng (冯济)[a,b,j,2], and Jian Wang[a,b,j,2]

[a]International Center for Quantum Materials, School of Physics, Peking University, 100871 Beijing, China; [b]Collaborative Innovation Center of Quantum Matter, 100871 Beijing, China; [c]Department of Physics, Pennsylvania State University, University Park, PA 16802; [d]Department of Physics, State Key Laboratory of Surface Physics, Fudan University, 200433 Shanghai, China; [e]Laboratory of Advanced Materials, Fudan University, 200433 Shanghai, China; [f]Science and Technology on Surface Physics and Chemistry Laboratory, 621908 Mianyang, China; [g]High Magnetic Field Laboratory, Chinese Academy of Sciences, 230031 Hefei, Anhui, China; [h]Department of Materials Science and Engineering, State Key Laboratory of Silicon Materials, Center of Electron Microscopy, Zhejiang University, 310027 Hangzhou, China; [i]Collaborative Innovation Center of Advanced Microstructures, 210093 Nanjing, China; and [j]Chinese Academy of Science Center for Excellence in Topological Quantum Computation, University of Chinese Academy of Sciences, 100190 Beijing, China

Topological Weyl semimetals (TWSs) with pairs of Weyl points and topologically protected Fermi arc states have broadened the classification of topological phases and provide superior platform for study of topological superconductivity. Here we report the nontrivial superconductivity and topological features of sulfur-doped T_d-phase MoTe$_2$ with enhanced T$_c$ compared with type-II TWS MoTe$_2$. It is found that T_d-phase S-doped MoTe$_2$ (MoTe$_{2-x}$S$_x$, $x \sim 0.2$) is a two-band s-wave bulk superconductor (∼0.13 meV and 0.26 meV), where the superconducting behavior can be explained by the s_{+-} pairing model. Further, measurements of the quasi-particle interference (QPI) patterns and a comparison with band-structure calculations reveal the existence of Fermi arcs in MoTe$_{2-x}$S$_x$. More interestingly, a relatively large superconducting gap (∼1.7 meV) is detected by scanning tunneling spectroscopy on the sample surface, showing a hint of topological nontrivial superconductivity based on the pairing of Fermi arc surface states. Our work demonstrates that the T_d-phase MoTe$_{2-x}$S$_x$ is not only a promising topological superconductor candidate but also a unique material for study of s_{+-} superconductivity.

T_d MoTe$_{2-x}$S$_x$ | Weyl semimetal | s_{+-} superconductivity | topological superconductivity

Topological Dirac semimetals (TDSs) and topological Weyl semimetals (TWSs) have been shown to host the condensed-matter physics counterpart of relativistic fermions in quantum-field theory (1, 2). Their low-energy quasi-particle states with linear dispersion can be effectively described by the Dirac equation and the Weyl equation, respectively. They are also characterized by nontrivial topological invariants, broadening the classification of topological phases of condensed matter beyond topological insulators (3–13). In contrast to relativistic fermions which need to respect Lorentz invariance, the less constrained condensed-matter systems feature some excitations that have no analogy in high-energy physics. One of the most fascinating quasi-particles in this context exists in type-II TWSs whose Weyl cones are strongly tilted (14–16). In contrast to the point-like bulk Fermi surfaces formed in type-I TDSs and TWSs, these type-II TWSs harbor a finite density of states at the Fermi level.

Topological materials that host superconductivity are ideal systems to detect topological superconductivity and Majorana fermions (17–23). In time-reversal symmetric Weyl semimetals, theory predicts that time-reversal symmetric topological superconductivity can arise from sign-changing superconductivity in Fermi surfaces with different Chern numbers (20). In addition, the superconductivity of topological surface states in TWSs may offer a new opportunity to study topological superconductivity (21) beyond the proximity-effect–induced superconducting surface states of topological insulators.

Other than being a type-II TWS with four pair of Weyl points (WPs) and Fermi arcs (24–30), T_d-MoTe$_2$ as a transition metal dichalcogenide material is found to be superconducting around 0.1 K (31). Understanding the superconductivity and topological properties of T_d-MoTe$_2$ is important for elucidating and exploiting topological superconductivity. However, the ultralow T$_c$ has limited the widespread study of superconductivity in T_d-MoTe$_2$. Recent studies of MoTe$_2$ have reported dome-shaped curves of T$_c$ vs. pressure and T$_c$ vs. sulfur concentration (31, 32). High-pressure studies of T_d-MoTe$_2$ suggest the possibility of emergence of a topological s_{+-} superconducting order parameter (33), although it is challenging to fully detect the topological properties in such high-pressure measurements. Here, we report a systematic study of superconductivity and topological properties of MoTe$_{2-x}$S$_x$ ($x \sim 0.2$ in this paper), wherein the T$_c$ is significantly enhanced to 1.27 K. According to our detailed transport and specific heat experiments, MoTe$_{2-x}$S$_x$ is a two-band s-wave bulk superconductor. Our results indicate possible s_{+-} rather than conventional s-wave superconductivity in this material as the interband coupling is stronger than the intraband

Significance

Searching for topological superconductors is of paramount importance in condensed-matter physics and materials science today: these materials are expected to harbor Majorana fermions on the edge states, an essential component for topological quantum computation platform. We experimentally observed s_{+-} pairing two-gap superconductivity and type-II Weyl semimetal property in T_d-phase MoTe$_{2-x}$S$_x$ ($x \approx 0.2$). Further, an enhanced surface superconducting gap comparing to bulk gaps is discovered. Our findings are strongly suggestive of topological superconductivity of the T_d-phase MoTe$_{2-x}$S$_x$. This work not only presents an important breakthrough in searching for topological superconductors but also inspires further investigations on the sign-change superconductivity beyond Fe-based high-T$_c$ superconductors.

PHYSICS

coupling. By scanning tunneling spectroscopy (STS), we observed quasi-particle interference (QPI) patterns that are consistent with the existence of Fermi arcs. Further calculations reveal that $MoTe_{2-x}S_x$ is a type-II TWS with Fermi arcs and four pairs of WPs at 5 meV (W1) and 50 meV (W2), respectively. The surface superconducting gap (Δ) found by STS is 1.70 meV at 0.4 K, which is much larger than bulk superconducting gaps and gives a huge gap to critical temperature ratio (at least 8.6) comparing to the conventional BCS (Bardeen–Cooper–Schrieffer) ratio of 1.76, thus suggesting a signature of unconventional superconductivity. In topological systems with s-wave bulk superconductivity, the topological surface states can form odd parity superconductivity (18). The relatively large superconducting gap detected by STS here hints nontrivial superconductivity from the topological surface states.

Results

Two-Band Superconductivity Detected by Magnetotransport Measurements.

$MoTe_2$ crystallizes in the $1T'$ phase (monoclinic, $P2_1/m$) at room temperature and transitions into the T_d phase (orthorhombic, $Pmn2_1$) at low temperature. We synthesized $MoTe_{2-x}S_x$ single crystals by the chemical vapor transport method and characterized them using optical microscopy, cross-sectional scanning transmission electron microscopy (STEM), X-ray diffraction, and scanning tunneling microscopy (STM). In Fig. 1*A*, the atomically resolved high-angle annular dark-field (HAADF) STEM image manifests the high-quality nature of our $MoTe_{2-x}S_x$ single crystal, showing the same atomic structure as intrinsic $MoTe_2$ (31). Fig. 1*B* is the (001) surface topography scanned by STM under 4.2 K. We carried out a series of transport experiments that mapped out the resistivity of our samples under various temperatures and magnetic fields using a standard four-probe method in a 16T-Physical Property Measurement System (PPMS) from Quantum Design. The current was applied along the Mo chains (*a* axis) (Fig. 1*C*). *SI Appendix*, Fig. S5 shows the typical temperature dependence of the four-probe resistivity

from 300 K down to 10 K under zero magnetic field. Around 189 K, there is a peak in the first-order differentiation of the ρ(T) curve, indicating the structural transition from the $1T'$ phase to the T_d phase (*SI Appendix*, Fig. S5*A*). Compared with undoped $MoTe_2$, the structural transition temperature is lowered to 189 K from 250 K by doping and the resistivity anomaly hysteresis between cooling down and warming up measurements is weaker (31). The zero-resistivity superconductivity transition temperature $T_c = 1.27$ K is obtained by extrapolating the superconductivity transition curve (Fig. 1*D*). We define the onset superconductivity transition temperature, $T_c^{onset} = 2.3$ K, at which ρ(T) diverges from its extrapolated normal state (Fig. 1*D*). $T_c^{middle} = 1.57$ K is determined at the temperature where the resistivity drop reaches 50% of ρ_n. ρ_n is the resistivity taken at 4 K without an external magnetic field.

To explore the superconductivity nature of $MoTe_{2-x}S_x$, we conducted systematic magnetotransport measurements under a perpendicular field $H^\perp$ (along the *c* axis) at different temperatures (Fig. 2*A*). The upper critical field (H_{c2}) is defined as the value at which the resistivity drop reaches 50% of ρ_n. The temperature dependence of $H_{c2}^\perp$ is shown in Fig. 2*B*. At 0.5 K, the parallel critical field $H_{c2}^\parallel$ (which is 21.7 kOe along *b* axis, *SI Appendix*, Fig. S6) is 6.6 times of the $H_{c2}^\perp$(3.3 kOe). This is a typical characteristic of layered superconductors. Both $H_{c2}^\perp$ and $H_{c2}^\parallel$ are below the Pauli limit field $H_p(0) = 1.86T_c^{middle} = 29.2$ kOe.

Interestingly, there is a slight upturn of the critical magnetic field near T_c. Furthermore, when the temperature approaches 80 mK, the observed $H_{c2}^\perp$ is enhanced compared with the standard single-band s-wave Werthamer–Helfand–Hohenberg (WHH) model (34) as shown by the pink line in Fig. 2*B*. This enhancement of $H_{c2}^\perp$ at low temperature implies that the two-band effect is not negligible (35). The two-band superconducting behavior has been observed in MgB_2 and Fe-based superconductors. Taking the orbital pair-breaking effect into account and ignoring the interband scattering, H_{c2} (T) can be expressed by ref. 35.

$$a_0[\ln t + U(h)][\ln t + U(\eta h)] + a_2[\ln t + U(\eta h)] + a_1[\ln t + U(h)] = 0$$

$$t = \frac{T}{T_c}, U(x) = \psi\left(\frac{1}{2} + x\right) - \psi(x)$$

$$\eta = \frac{D_2}{D_1}; \quad h = \frac{H_{c2}D_1}{2\varphi_0 T}; \quad a_0 = \frac{2\varpi}{\lambda_0}; \quad a_1 = 1 + \frac{\lambda_-}{\lambda_0}; a_2 = 1 - \frac{\lambda_-}{\lambda_0}$$

$$\varpi = \lambda_{11}\lambda_{22} - \lambda_{12}\lambda_{21}; \lambda_0 = \left(\lambda_-^2 + 4\lambda_{12}\lambda_{21}\right)^{1/2}; \lambda_- = \lambda_{11} - \lambda_{22}.$$

[1]

$\psi(x)$ is the digamma function. D_1 and D_2 are intraband diffusivities of bands 1 and 2, and φ_0 is the magnetic flux quantum. The parameters a_0, a_1, and a_2 are constants described with intraband and interband coupling strength. Terms λ_{11} and λ_{22} are the intraband couplings in bands 1 and 2. λ_{12} and λ_{21} describe the interband couplings between bands 1 and 2. This expression of H_{c2} is derived from the Eliashberg equation in which the microscopic details of different bands are described by the normal-state electronic diffusivity tensors D_m for each Fermi surface sheet. The diffusivity ratio η determines the curvature of H_{c2}(T) curve. We note that when $\eta = 1$, this equation will be reduced to the simplified single-band WHH model. Here, D_2 equals $141D_1$, which suggests a significant difference in the electron mobility in the two bands of $MoTe_{2-x}S_x$. The red line in Fig. 2*B* shows a fit of the experimental data with Eq. 1. The fitting parameters are $\lambda_{11} = 9.7$, $\lambda_{12} = 2.6$, $\lambda_{21} = 2.6$, $\lambda_{22} = 0.5$, $D_1 = 0.076$, $D_2 = 10.7$, $C = 1.015$, $\varpi = -1.91$.

Two-Band s-Wave Bulk Superconductivity Confirmed by Diamagnetism and Specific Heat Measurements.

We obtain additional insights using magnetization measurements of the diamagnetism in the crystals using a Quantum Design Magnetic Property Measurement
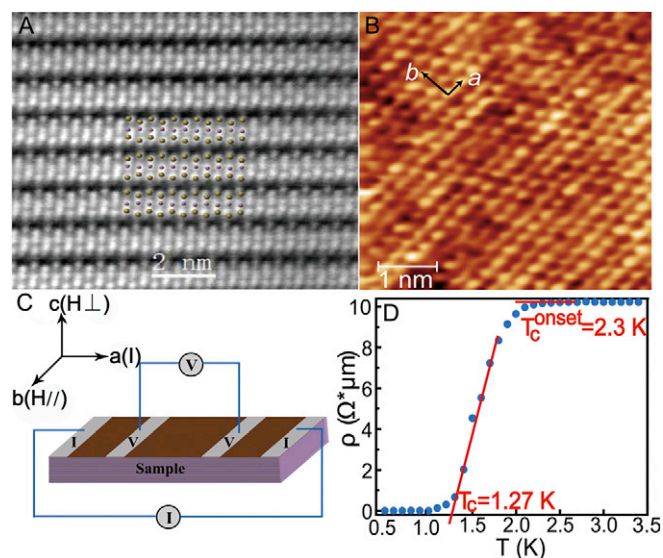
Fig. 1. Characterization of $MoTe_{2-x}S_x$ and schematic structure for electrical transport measurements. (*A*) A high-resolution HAADF-STEM image of $MoTe_{2-x}S_x$ single crystal taken along the (100) zone axis. The gray spheres simulate the atoms. (*B*) STM image of cleaved (001) surface of $MoTe_{2-x}S_x$, showing atomically resolved lattice. The surface unit cell is indicted by black arrows with lattice constant of a = 3.5 Å and b = 6.3 Å. (*C*) Schematic structure for electrical transport measurements in $MoTe_{2-x}S_x$. (*D*) Typical resistivity–temperature curve of $MoTe_{2-x}S_x$ showing superconductivity.
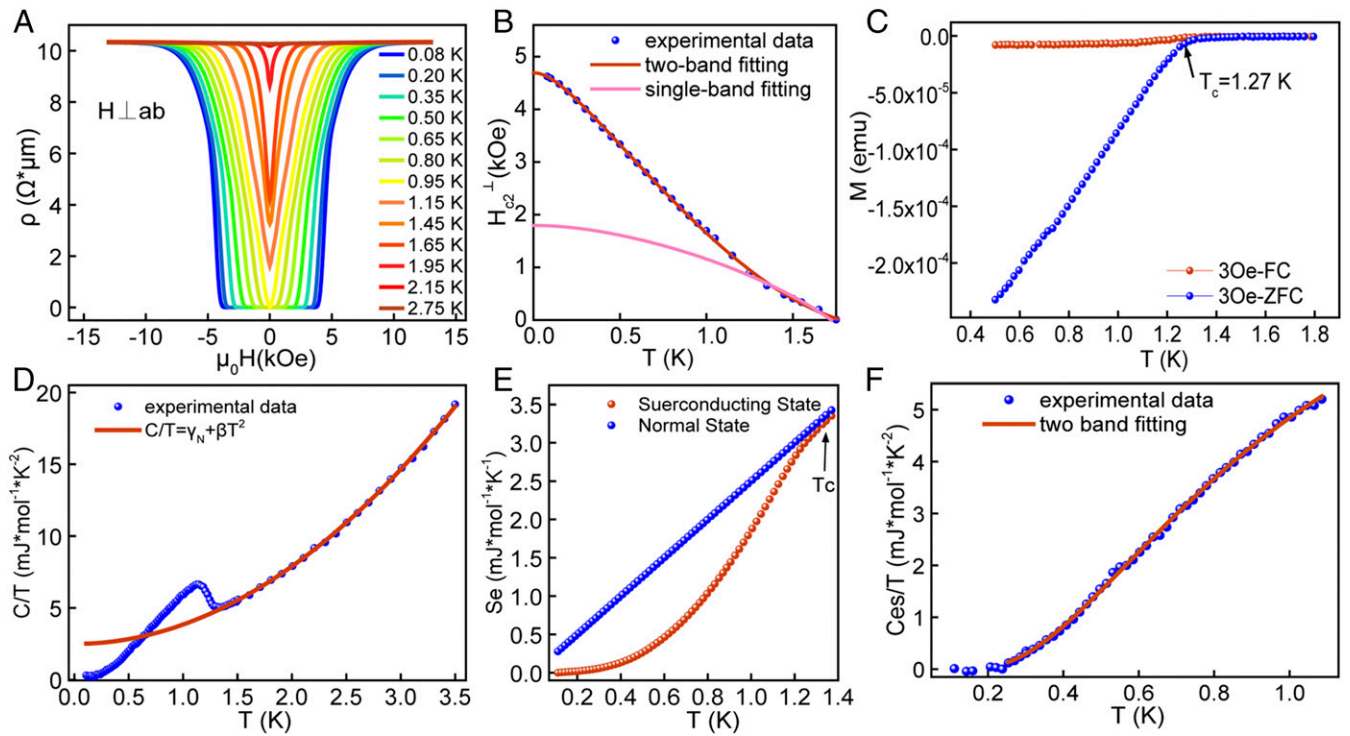
Fig. 2. Superconducting properties of MoTe$_{2-x}$S$_x$ in low-temperature regime. (*A*) Magnetoresistance at various temperatures under perpendicular field. (*B*) Temperature dependence of H$_{c2}^{\perp}$. The pink curve and red curve are the best fit of single-band *s*-wave WHH model and two-band *s*-wave model to the experimental data, respectively. (*C*) Magnetization behavior measured under a 3-Oe magnetic field parallel to the (001) sample surface, showing the Meissner effect. (*D*) Temperature dependence of specific heat divided by temperature C/T for MoTe$_{2-x}$S$_x$ single crystal in zero field. The red line represents the best fit to C/T = $\gamma_n + \beta T^2$. (*E*) The entropy in the normal and superconducting states as a function of temperature. (*F*) The electronic specific heat C$_{es}$/T as a function of temperature. The red line represents the fit of C$_{es}$/T below T$_c$ using the two-band *s*-wave model.

System (MPMS 7-XL SQUID), with a resolution of 10^{-8} EMU. Fig. 2*C* shows the dc magnetization curves as a function of temperature during zero-field cooling and field cooling under H$^{\parallel}$ = 3 Oe. An apparent drop appears below 1.27 K, indicating the superconducting Meissner effect below T$_c$.

To further study the superconducting behavior of our sample, we also conducted specific heat measurements in PPMS. Fig. 2*D* displays the C(T)/T curves of the MoTe$_{2-x}$S$_x$ single crystal down to 0.1 K at zero field. We observe a clear anomaly corresponding to the superconducting transition around 1.27 K, consistent with the T$_c$ observed in diamagnetic measurements (Fig. 2*C*) and transport measurements (Fig. 1*D*). The normal-state specific heat can be described by C(T) = C$_e$(T) + C$_{lattice}$(T) with electronic contribution of C$_e$(T) = γ_nT and the phonon contribution of C$_{lattice}$(T) = βT^3. The red line in Fig. 2*D* is the best fit to the C/T, yielding γ_n = 2.49 mJ·mol^{-1}·K^{-2} and β = 1.35 mJ·mol^{-1}·K^{-4} and a residual value γ_r = 0.2 mJ·mol^{-1}·K^{-2} (*SI Appendix*, Fig. S8). And, the superconducting volume ratio is 92% [($\gamma_n - \gamma_r$)/$\gamma_n \sim 92\%$], which manifests the bulk superconductivity of MoTe$_{2-x}$S$_x$. With the normal-state electronic specific heat derived from this fit, the entropy in the normal and superconducting states agrees with ($\int_0^{T_c}$(C$_e$/T)dT = γ_nT$_c$) within 1% deviation near the superconducting transition, for which the entropy conservation is confirmed to be satisfied in Fig. 2*E*. Considering the existence of γ_r, the electronic specific heat for one mole of superconducting material can be defined as C$_{es}$ = (C$_e$ − γ_nT)γ_n/($\gamma_n - \gamma_r$). Here in MoTe$_{2-x}$S$_x$, the C$_{es}$(T)/T can be fitted very well using a two-band *s*-wave superconductivity model C$_{es}$/T $\propto pe^{(-\Delta_1)/k_BT} + (1-p)e^{(-\Delta_2)/k_BT}$, in which Δ_i is the superconducting gap and *p* is a fitting parameter representing the weight of the total electron density of states for each band. Fig. 2*F* shows that the data are well described by this model with fitting parameter *p* = 0.3 [the gap values at zero temperature are

$\Delta_1 = 1.22k_BT_c$ (0.13 meV) and $\Delta_2 = 2.42k_BT_c$ (0.26 meV)]. This is consistent with the theoretical constraints that one gap must be larger than the BCS gap and one smaller in a weakly coupled two-band superconductor, as observed in MgB$_2$. Note that muon spin rotation experiments show that the values of the gaps in our MoTe$_{2-x}$S$_x$ are almost the same as those of MoTe$_2$ under 0.45 GPa high pressure (33).

Calculations of Band Structure. As shown above, our transport, diamagnetism, and specific heat measurements demonstrate two-band *s*-wave bulk superconductivity in MoTe$_{2-x}$S$_x$. To explore the topological property of MoTe$_{2-x}$S$_x$, we examined its band structure and surface states (Fermi arcs) with x = 0.2 by first-principles calculation. As detailed in *Materials and Methods*, tight-binding models are obtained to describe the electronic structure of MoTe$_{2-x}$S$_x$ and the **k**-dependent surface spectral function by an iterative projection procedure (36). The Fermi surfaces of MoTe$_{2-x}$S$_x$ are mainly located in the central region of the surface Brillouin zone (BZ) except for a small electron pocket near the $\overline{Y}$ point. Here, we focus on the central region of the BZ which covers all of the bulk WPs. Fig. 3*A* shows the surface spectral function at Fermi level E$_F$. Bowtie-shaped hole pockets appear near $\overline{\Gamma}$, and electron pockets appear along the path $\overline{\Gamma} - \overline{X}$. According to Fig. 3 *B* and *C*, the above observed electron and hole pockets touch each other at eight WPs at ~E$_F$ + 5 meV (W$_1$) and ~E$_F$ + 50 meV (W$_2$), respectively. Topological Fermi arcs (highlighted by red arrows in Fig. 3 *B* and *C*) connecting the WPs with opposite chirality, emerges from W$_1$ point and ends at W$_2$ point. The Fermi arc roughly spans 5% of the BZ. Additionally, there are trivial surface states (indicated by red arrows in Fig. 3 *B* and *C*) which form a closed loop and merge partially with the bulk electron

Fig. 3. Calculated Fermi surfaces of MoTe$_{2-x}$S$_x$. (*A*) Calculated spectral function at E$_F$ (*B*) Spectral function at 0.005 eV. (*C*) Spectral function at 0.05 eV. The range of momentum of *B* and *C* is marked by the red rectangle in *A*. The Weyl points and topological Fermi arcs are pointed out in *B* and *C*.

pocket. Clearly, the Fermi surfaces of MoTe$_{2-x}$S$_x$ have almost the same features as undoped MoTe$_2$ with little modulation of WPs' energies and positions.

QPI Measurements of Fermi Arcs. To verify the nontrivial electron states of MoTe$_{2-x}$S$_x$, we performed low-temperature STM measurements (*Materials and Methods*). The topographic image of a cleaved MoTe$_{2-x}$S$_x$ crystal shows atomically flat terraces with stripe-like structure along the *a* axis (Fig. 1*B*), similar to undoped MoTe$_2$ (26). We carried out differential conductance (dI/dV) maps (with spatial resolution at various energies) on such surfaces; this is expected to reveal the QPI patterns generated by surface states. The dI/dV maps are taken within a 50 nm × 50-nm area at various energies at T = 4.2 K (*SI Appendix*, *Fig. S4*). Their corresponding fast Fourier transforms (FFT) are shown in Fig. 4 *A–F*. One can clearly see the dumbbell-like scattering patterns in these FFT images, similar to that obtained on undoped MoTe$_2$ (26) and Mo$_{1-x}$W$_x$Te$_2$ (37).

To understand the origin of these patterns, we simulated the QPI by calculating the joint density of states (JDOS):

$$J(\mathbf{q}, \omega) = \sum_{\mathbf{k}} A(\mathbf{k}, \omega) A(\mathbf{k} + \mathbf{q}, \omega). \qquad [2]$$

Here, $A(\mathbf{k}, \omega)$ is the **k**-dependent surface spectral function and $\hbar\omega$ is the energy of the Bloch electron, and the scattering vector **q** considered here is located only in the first BZ. The calculated JDOS are shown in Fig. 4 *G–L*. The dumbbell pattern is well reproduced in the simulations. To have a more quantitative comparison, a simplified scattering geometry is sketched in Fig. 4*M*, in which q1 and q2 connect Fermi arcs and q3 connects trivial surface states. In Fig. 4*N*, we extracted the dispersion of the dumbbell pattern (by taking FFT profiles along the line marked in Fig. 4*A*), and the calculated dispersion of q1~q3 are superposed. We find that the experimental dispersion has a similar trend with q1~q3, while the strongest scattering weight lies between q1, q3, and q2. This implies the observed scattering is possibly a superposition of q1, q2, and q3. In *SI Appendix*, *Fig. S9C*, it is shown that the calculations indicate significant contribution of Fermi arc states to the QPI scattering in the experimental range of bias potential. Thus, the QPI measurements indicate the coexistence of topological Fermi arcs and trivial surface states.

STS Detection of the Superconductivity. To further study the superconducting state of MoTe$_{2-x}$S$_x$, we performed STS measurement at temperatures below T$_c$. Fig. 5*A* is a typical dI/dV spectrum taken at T = 0.4 K on the surface shown in Fig. 1*B*. We observe a superconducting gap of 1.70 meV; for comparison, there is no gap feature in the STS taken at 4.2 K (see also Fig. 5*A*). Fig. 5*C* shows the magnetic field dependence of the STS taken on the same spot. At elevated fields, the gap is gradually filled up and vanishes under a field of 8 kOe, confirming its origin in superconductivity. This critical magnetic field measured by STM is consistent with the value obtained by transport measurements (the onset critical field shown in Fig. 2*A*). We note that the line shape of the observed gap cannot be fitted well by BCS theory. For comparison, we plot the calculated DOS of an isotropic BCS gap (dashed curve in Fig. 5*B*) with Δ = 1.7 meV and T$_{eff}$ = 1.18 K as the broadening factor (effective temperature of our system). The calculated gap significantly differs from the measured spectrum.

Fig. 4. Quasi-particle interference patterns of MoTe$_{2-x}$S$_x$. (*A–F*) The Fourier transform of the dI/dV maps taken at various energies. The Bragg points $(2\pi/b, 0)$ are indicated by white arrows. (*G–L*) Calculated JDOS (simulation of QPI) at different energies with respect to E$_F$. The dumbbell-like patterns are the main feature of Fermi arcs in experimental QPI patterns and calculation results. (*M*) Sketch of extremal scattering wave vectors between Fermi arcs (q1 and q2) and trivial surface states (q3). (*N*) Dispersions extracted from QPI by taken line cut along the line marked in *A*. The calculated dispersions of q1, q2, and q3 are superposed for comparison.

Fig. 5. Superconducting gap on the surface of $MoTe_{2-x}S_x$ measured by STM. (A) dI/dV spectrum taken on $MoTe_{2-x}S_x$ sample at 4.2 K (blue curve) and 0.4 K (red curve), respectively. A superconducting gap with $\Delta = 1.7$ meV (as marked) was clearly observed at 0.4 K. (B) Comparison of the measured gap (red curve) with a simulated isotropic BCS gap (dashed curve). (C) dI/dV spectra measured at 0.4 K under various magnetic fields. The gap was obviously suppressed with increasing external magnetic field and the critical magnetic field is 8 kOe.

Discussion

There are two kinds of scenarios for two-band s-wave superconductivity: (i) conventional s-wave pairing dominated by strong intraband coupling $\varpi > 0$ and (ii) strong interband coupling $\varpi < 0$ which can result in the π shift between the order parameter on two bands (s_{+-} pairing) (38, 39). Here, in our fitting $\varpi = -1.91$, which supports sign-change superconductivity in $MoTe_{2-x}S_x$ single crystal, i.e., s_{+-} Cooper pairing. Some Fe-based superconductors (Fe-SCs) have already been predicted and proven to be s_{+-} superconductors. The hole carrier and electron carrier in Fermi surface of Fe-SCs carry the opposite superconducting gap phase. It is believed that spin fluctuations are responsible for the interaction that induces sign-change superconductivity in different Fermi surfaces for Fe-SCs (40, 41). Although hole carriers and electron carriers also coexist in $MoTe_{2-x}S_x$, phonons provide the principal interaction for Cooper pairing in $MoTe_{2-x}S_x$. This view is supported by the fact that S doping enhances the T_c significantly (32) and that there is no magnetic order in $MoTe_2$ (33). Further, S doping is not supposed to induce magnetic order. Therefore, the origin of the interaction that contributes to the sign-change superconductivity in $MoTe_{2-x}S_x$ is quite mysterious. Moreover, this kind of sign change of the superconducting gap function between different Fermi surfaces in time-reversal invariant TWS can lead to topological superconductivity.

In addition, the surface superconducting gap size observed by STM ($\Delta = 1.7$ meV) is surprisingly large compared with the T_c of $MoTe_{2-x}S_x$. By transport measurements (Fig. 1D), the resistance starts to drop at 2.3 K and reaches zero at 1.27 K. Even if we take 2.3 K as the onset T_c, the BCS ratio (Δ/k_BT_c) is 8.6. This value is much larger than that of the conventional weak-coupling superconductors (1.76), and also larger than the fitting results from our specific heat measurement (1.22 and 2.42). Besides, the line shape of this gap cannot be fitted well by BCS theory. One possible explanation of the unexpected large gap is that it may stem from the topological surface states of $MoTe_{2-x}S_x$. It was predicted that in a superconducting topological system with bulk s-wave pairing, a superconducting gap enhancement can occur on the surface states by anomalous

parity mixing (18). Intriguingly, recent experiments have shown an enhanced superconducting gap associated with the surface states of β-Bi_2Pd films (The surface superconducting gap is 2.15 meV, while the bulk superconducting gap is 1 meV.) (42). Thus, we speculate that the observed large gap may be related to the Fermi arc surface states of $MoTe_{2-x}S_x$. Further experimental and theoretical studies are still needed to clarify its origin.

Conclusion

In summary, we report the discovery of nontrivial superconductivity and topological behavior in T_d phase $MoTe_{2-x}S_x$ single crystals. Our transport and specific heat measurements show potential s_{+-}-wave two-band superconductivity arising from a dominant interband coupling. The s_{+-} paring of TWS $MoTe_{2-x}S_x$ makes the material a topological superconductor candidate. Moreover, the observed QPI patterns of Fermi arcs are consistent with the calculated nontrivial band structure. In addition, we have detected a relatively large superconducting gap on the sample surface, potentially indicating odd pairing superconductivity from Fermi arc surface states. This kind of s-wave bulk superconductor with Fermi arcs provides a unique platform to investigate topological superconductivity. More interestingly, the weak interlayer van der Waals coupling in this material makes it attractive for potential applications of TWS and superconductor devices.

Materials and Methods

Crystal Growth. The growth of $MoTe_{2-x}S_x$ single crystals used for this study has been previously reported (32). Using iodine as the transport agent, $1T'$ single crystals of $MoTe_{2-x}S_x$ were grown by vapor transport method and then quenched in ice water to yield the high-temperature monoclinic phase. First, stoichiometric amounts of Mo, Te, and S were ground and pressed into pellets and then heated in an evacuated quartz tube at 810 °C for 7 d to get polycrystalline $MoTe_{2-x}S_x$ powder. Then, the powder was sealed in a evacuated quartz tube flushed by Ar and heated with I_2 in a two-zone furnace with the hot zone kept at 1,010 °C and cold zone kept at 910 °C. The single crystal is characterized by various methods as shown in the main text. The concentration of S in single crystal samples is decided by energy-dispersive spectroscopy.

Electronic Structure Calculation. Density-functional theory calculations were performed using the projector-augmented wave method as implemented in the Vienna ab initio simulation package (VASP) (43) within the generalized gradient approximation parametrized by Perdew, Burke, and Ernzerhof. The energy cutoff is set to 450 eV for a plane-wave basis and the k-point mesh is taken as $12 \times 6 \times 3$ for the bulk calculations. The spin-orbit coupling effect is self-consistently included. To calculate the surface and bulk electronic structure, we constructed a tight-binding Hamiltonian for both $MoTe_2$ and MoS_2, where the tight-binding model matrix elements were calculated by projecting onto the Wannier orbitals, which used the VASP2WANNIER90 interface (44). The lattice parameters of $MoTe_{2-x}S_x$ single crystal are shown in *SI Appendix, Text* and Fig. S2. We used Mo d orbitals and Te(S) p orbitals to construct Wannier functions without using the maximizing localization procedure. The electronic structure of the samples with finite doping was calculated by a linear interpolation of tight-binding model matrix elements of $MoTe_2$ and MoS_2. The surface state electronic structure was calculated by the surface Green's function technique (36).

STM Measurement. The STM experiment was conducted in a commercial Unisoku 1300 STM system at the temperature of 4.2 K and 0.4 K. $MoTe_{2-x}S_x$ samples were cleaved in ultrahigh vacuum at 100 K. PtIr tips were used in all measurements after careful treatment on a Au(111) surface. The tunneling spectroscopy (dI/dV) was performed using a standard lock-in technique with modulation frequency $f = 915$ Hz and typical amplitude $\Delta V = 1$ mV.

PHYSICS

1. Nielsen HB, Ninomiya M (1983) The Adler-Bell-Jackiw anomaly and Weyl fermions in a crystal. *Phys Lett B* 130:389–396.
2. Burkov AA (2016) Topological semimetals. *Nat Mater* 15:1145–1148.
3. Weng H, Dai X, Fang Z (2016) Topological semimetals predicted from first-principles calculations. *J Phys Condens Matter* 28:303001.
4. Lv BQ, et al. (2015) Observation of Weyl nodes in TaAs. *Nat Phys* 11:724–727.
5. Xu S-Y, et al. (2015) TOPOLOGICAL MATTER. Discovery of a Weyl fermion semimetal and topological Fermi arcs. *Science* 349:613–617.
6. Dai X (2016) Weyl semimetals: A group family picture. *Nat Mater* 15:5–6.
7. Young SM, et al. (2012) Dirac semimetal in three dimensions. *Phys Rev Lett* 108:140405.
8. Huang X, et al. (2015) Observation of the chiral-anomaly-induced negative magnetoresistance in 3D Weyl semimetal TaAs. *Phys Rev X* 5:031023.
9. Zhang C-L, et al. (2016) Signatures of the Adler-Bell-Jackiw chiral anomaly in a Weyl fermion semimetal. *Nat Commun* 7:10735.
10. Li Y, et al. (2016) Negative magnetoresistance in Weyl semimetals NbAs and NbP: Intrinsic chiral anomaly and extrinsic effects. *Front Phys* 12:127205.
11. Gooth J, et al. (2017) Experimental signatures of the mixed axial-gravitational anomaly in the Weyl semimetal NbP. *Nature* 547:324–327.
12. Burkov AA (2014) Anomalous Hall effect in Weyl metals. *Phys Rev Lett* 113:187202.
13. Potter AC, Kimchi I, Vishwanath A (2014) Quantum oscillations from surface Fermi arcs in Weyl and Dirac semimetals. *Nat Commun* 5:5161.
14. Soluyanov AA, et al. (2015) Type-II Weyl semimetals. *Nature* 527:495–498.
15. Wang Y, et al. (2016) Gate-tunable negative longitudinal magnetoresistance in the predicted type-II Weyl semimetal WTe₂. *Nat Commun* 7:13142.
16. Yu ZM, Yao Y, Yang SA (2016) Predicted unusual magnetoresponse in type-II Weyl semimetals. *Phys Rev Lett* 117:077202.
17. Fu L, Kane CL (2008) Superconducting proximity effect and majorana fermions at the surface of a topological insulator. *Phys Rev Lett* 100:096407.
18. Mizushima T, Yamakage A, Sato M, Tanaka Y (2014) Dirac-fermion-induced parity mixing in superconducting topological insulators. *Phys Rev B* 90:184516.
19. Sun H-H, et al. (2016) Majorana zero mode detected with spin selective Andreev reflection in the vortex of a topological superconductor. *Phys Rev Lett* 116:257003.
20. Hosur P, Dai X, Fang Z, Qi X-L (2014) Time-reversal-invariant topological superconductivity in doped Weyl semimetals. *Phys Rev B* 90:045130.
21. Chen A, Franz M (2016) Superconducting proximity effect and Majorana flat bands at the surface of a Weyl semimetal. *Phys Rev B* 93:201105.
22. He QL, et al. (2017) Chiral Majorana fermion modes in a quantum anomalous Hall insulator-superconductor structure. *Science* 357:294–299.
23. Wang H, et al. (2016) Observation of superconductivity induced by a point contact on 3D Dirac semimetal Cd₃As₂ crystals. *Nat Mater* 15:38–42.
24. Sun Y, Wu S-C, Ali MN, Felser C, Yan B (2015) Prediction of Weyl semimetal in orthorhombic MoTe₂. *Phys Rev B* 92:161107.
25. Wang Z, et al. (2016) MoTe_₂: A type-II Weyl topological metal. *Phys Rev Lett* 117: 056805.
26. Deng K, et al. (2016) Experimental observation of topological Fermi arcs in type-II Weyl semimetal MoTe₂. *Nat Phys* 12:1105–1110.
27. Jiang J, et al. (2017) Signature of type-II Weyl semimetal phase in MoTe₂. *Nat Commun* 8:13973.
28. Huang L, et al. (2016) Spectroscopic evidence for a type II Weyl semimetallic state in MoTe₂. *Nat Mater* 15:1155–1160.
29. Tamai A, et al. (2016) Fermi arcs and their topological character in the candidate type-II Weyl semimetal MoTe₂. *Phys Rev X* 6:031021.
30. Liang A, et al. (2016) Electronic evidence for type II Weyl semimetal state in MoTe₂. arXiv:1604.01706. Preprint, posted April 6, 2016.
31. Qi Y, et al. (2016) Superconductivity in Weyl semimetal candidate MoTe₂. *Nat Commun* 7:11038.
32. Chen FC, et al. (2016) Superconductivity enhancement in the S-doped Weyl semimetal candidate MoTe₂. *Appl Phys Lett* 108:162601.
33. Guguchia Z, et al. (2017) Signatures of the topological s₊₋ superconducting order parameter in the type-II Weyl semimetal T_d-MoTe₂. *Nat Commun* 8:1082.
34. Werthamer NR, Helfand E, Hohenberg PC (1966) Temperature and purity dependence of the superconducting critical field, H_{c2}. III. Electron spin and spin-orbit effects. *Phys Rev* 147:295–302.
35. Gurevich A (2003) Enhancement of the upper critical field by nonmagnetic impurities in dirty two-gap superconductors. *Phys Rev B* 67:184515.
36. Sancho MPL, Sancho JML, Sancho JML, Rubio J (1985) Highly convergent schemes for the calculation of bulk and surface Green functions. *J Phys F Met Phys* 15:851.
37. Zheng H, et al. (2016) Atomic-scale visualization of quasiparticle interference on a type-II Weyl semimetal surface. *Phys Rev Lett* 117:266804.
38. Jaroszynski J, et al. (2008) Upper critical fields and thermally-activated transport of NdFeAsO_{0.7}F_{0.3} single crystal. *Phys Rev B* 78:174523.
39. Mazin II, Singh DJ, Johannes MD, Du MH (2008) Unconventional superconductivity with a sign reversal in the order parameter of LaFeAsO_{1-x}F_x. *Phys Rev Lett* 101:057003.
40. Essenberger F, et al. (2016) Ab initio theory of iron-based superconductors. *Phys Rev B* 94:014503.
41. Nomura Y, Nakamura K, Arita R (2014) Effect of electron-phonon interactions on orbital fluctuations in iron-based superconductors. *Phys Rev Lett* 112:027002.
42. Lv Y-F, et al. (2017) Experimental signature of topological superconductivity and Majorana zero modes on β-Bi₂Pd thin films. *Sci Bull (Beijing)* 62:852–856.
43. Kresse G, Furthmüller J (1996) Efficient iterative schemes for ab initio total-energy calculations using a plane-wave basis set. *Phys Rev B Condens Matter* 54:11169–11186.
44. Franchini C, et al. (2012) Maximally localized Wannier functions in LaMnO₃ within PBE + U, hybrid functionals and partially self-consistent GW: An efficient route to construct ab initio tight-binding parameters for eg perovskites. *J Phys Condens Matter* 24:235602.